Research Article | Vol. 26, No. 18 | 3 Sep 2018 | OPTICS EXPRESS 24031
Optics EXPRESS

Ultra-broadband, polarization-independent, wide-angle absorption in impedance-matched metamaterials with anti-reflective moth-eye surfaces

Rushin Contractor,[1,*] Giuseppe D'Aguanno,[2] and Curtis Menyuk[1]

[1]*Department of Computer Science and Electrical Engineering, University of Maryland Baltimore County, Baltimore, MD 21250, USA*
[2]*Department of Electrical and Computer Engineering, The University of Texas at Austin, Austin, TX 78712, USA*
**contractorrushin@gmail.com*

Abstract: We computationally study periodic impedance-matched metal-dielectric metamaterials and the advantage of imprinting moth-eye surfaces on them. Impedance-matched metamaterials are known to act as strong, polarization-independent, broadband absorbers. However, in the infrared region far from the metal's plasma frequency, the reflection from metal layers dominates over the absorption. Using anti-reflective moth-eye surfaces we show that it is possible to obtain absorption independent of polarization or incidence angle, over an exceptionally broad frequency range from 400 nm to 6 μm.

OCIS codes: (160.3918) Metamaterials; (310.3915) Metallic, opaque, and absorbing coatings.

References and links

1. W. W. Salisbury, "Absorbent body for electromagnetic waves," US Patent 2599944 (1952).
2. V. G. Veselago, "The electrodynamics of substances with simultaneously negative values of ϵ and μ," Phys. Usp. **10**, 509–514 (1968).
3. R. A. Shelby, D. R. Smith, and S. Schultz, "Experimental verification of a negative index of refraction," Science **292**, 77–79 (2001).
4. N. I. Landy, S. Sajuyigbe, J. J. Mock, D. R. Smith, and W. J. Padilla, "Perfect metamaterial absorber," Phys. Rev. Lett. **100**, 207402 (2008).
5. H. Tao, N. I. Landy, C. M. Bingham, X. Zhang, Richard D. Averitt, and Willie J. Padilla, "A metamaterial absorber for the terahertz regime: Design, fabrication and characterization," Opt. Express **16**, 7181–7188 (2008).
6. X. Liu, T. Starr, A. F. Starr, and W. J. Padilla, "Infrared spatial and frequency selective metamaterial with near-unity absorbance," Phys. Rev. Lett. **104**, 207403 (2010).
7. K. Aydin, V. E. Ferry, R. M. Briggs, and H. A. Atwater, "Broadband polarization-independent resonant light absorption using ultrathin plasmonic super absorbers," Nat. Commun. **2**, 571 (2011).
8. Hao Wang and Liping Wang, "Perfect selective metamaterial solar absorbers," Opt. Express **21**, A1078–A1093 (2013).
9. C. Wu, B. Neuner III, J. John, A. Milder, B. Zollars, S. Savoy, and G. Shvets, "Metamaterial-based integrated plasmonic absorber/emitter for solar thermo-photovoltaic systems," J. Opt. **14**, 024005 (2012).
10. A. Ghanekar, L. Lin, and Y. Zheng, "Novel and efficient Mie-metamaterial thermal emitter for thermophotovoltaic systems," Opt. Express **24**, A868–A877 (2016).
11. H. Yu, Z. Zhao, Q. Qian, J. Xu, P. Gou, Y. Zou, J. Cao, L. Yang, J. Qian, and Z. An, "Metamaterial perfect absorbers with solid and inverse periodic cross structures for optoelectronic applications," Opt. Express **25**, 8288–8295 (2017).
12. N. Liu, M. Mesch, T. Weiss, M. Hentschel, and H. Giessen, "Infrared perfect absorber and its application as plasmonic sensor," Nano Lett. **10**, 2342–2348 (2010).
13. K. Iwaszczuk, A. C. Strikwerda, K. Fan, X. Zhang, R. D. Averitt, and P. Uhd Jepsen, "Flexible metamaterial absorbers for stealth applications at terahertz frequencies," Opt. Express **20**, 635–643 (2012).
14. Y. Shi, Y. C. Li, T. Hao, L. Li, and C. Liang, "A design of ultra-broadband metamaterial absorber," Wave Random Complex **27**, 381–391 (2017).
15. J. Zhu, Z. Ma, W. Sun, F. Ding, Q. He, L. Zhou, and Y. Ma, "Ultra-broadband terahertz metamaterial absorber," Appl. Phys. Lett. **105**, 021102 (2014).

#334729 https://doi.org/10.1364/OE.26.024031
Journal © 2018 Received 26 Jun 2018; revised 1 Aug 2018; accepted 21 Aug 2018; published 31 Aug 2018

Optics EXPRESS

16. Y. K. Zhong, Y. Lai, M. Tu, B. Chen, S. M. Fu, P. Yu, and A. Lin, "Omnidirectional, polarization-independent, ultra-broadband metamaterial perfect absorber using field-penetration and reflected-wave-cancellation," Opt. Express **24**, A832–A845 (2016).
17. N. Mattiucci, M. J. Bloemer, N. Akozbek, and G. D'Aguanno, "Impedance matched thin metamaterials make metals absorbing," Sci. Rep. **3**, 3203 (2013).
18. N. Mattiucci, G. D'Aguanno, N. Akozbek, M. Scalora, and M. J. Bloemer, "Homogenization procedure for a metamaterial and local violation of the second principle of thermodynamics," Opt. Commun. **283**, 1613–1620 (2010).
19. H. A. Macleod, *Thin-film optical filters* (CRC, Boca Raton, 2010).
20. Z.-P. Yang, L. Ci, J. A. Bur, S.-Y. Lin, and P. M. Ajayan, "Experimental observation of an extremely dark material made by a low-density nanotube array," Nano Lett. **8**, 446–451 (2008).
21. M. C. Larciprete, M. Centini, R. L. Voti, and C. Sibilia, "Selective and tunable thermal emission in metamaterials composed of oriented polar inclusions," J. Opt. Soc. Am. B **34**, 1459–1464 (2017).
22. C. G. Bernhard and W. H. Miller, "A corneal nipple pattern in insect compound eyes," Acta Physiol. Scand. **56**, 385–386 (1962).
23. D. Stavenga, S. Foletti, G. Palasantzas, and K. Arikawa, "Light on the moth-eye corneal nipple array of butterflies," Proc. Royal Soc. B, **273**, 661–667 (2006).
24. S. Chattopadhyay, Y. F. Huang, Y. J. Jen, A. Ganguly, K. H. Chen, and L. C. Chen, "Anti-reflecting and photonic nanostructures," Mater. Sci. Eng. R **69**, 1–35 (2010).
25. K.-C. Park, H. J. Choi, C.-H. Chang, R. E. Cohen, G. H. McKinley, and G. Barbastathis, "Nanotextured silica surfaces with robust superhydrophobicity and omnidirectional broadband supertransmissivity," ACS Nano **6**, 3789–3799 (2012).
26. Q. Yang, X. A. Zhang, A. Bagal, W. Guo and C.-H. Chang, "Antireflection effects at nanostructured material interfaces and the suppression of thin-film interference," Nanotechnology **24**, 235202 (2013).
27. R. J. Weiblen, C. R. Menyuk, L. E. Busse, L. B. Shaw, J. S. Sanghera, and I. D. Aggarwal, "Optimized moth-eye anti-reflective structures for As2S3 chalcogenide optical fibers," Opt. Express **24**, 10172–10187 (2016).
28. G. Tan, J. Lee, Y. Lan, M. Wei, L. Peng, I. Cheng, and S. Wu, "Broadband antireflection film with moth-eye-like structure for flexible display applications," Optica **4**, 678–683 (2017).
29. S.Y. Chou, P. R. Krauss, and P. J. Renstrom, "Nanoimprint lithography," J. Vac. Sci. Technol. B **14**, 4129–4133 (1996).
30. M. Kowalczyk, J. Haberko, and P. Wasylczyk, "Microstructured gradient-index antireflective coating fabricated on a fiber tip with direct laser writing," Opt. Express **22**, 12545–12550 (2014).
31. M. G. Moharam and T. K. Gaylord, "Rigorous coupled-wave analysis of planar-grating diffraction," J. Opt. Soc. Am. **71**, 811–818 (1995).
32. L. Li, "Formulation and comparison of two recursive matrix algorithms for modeling layered diffraction gratings," J. Opt. Soc. Am. A **13**, 1024-1035 (1996).
33. L. Li, "New formulation of the Fourier modal method for crossed surface-relief gratings," J. Opt. Soc. Am. A **14**, 2758–2767 (1997).
34. R. Rumpf, "Improved formulation of scattering matrices for semi-analytical methods that is consistent with convention," PIER B **35**, 241–261 (2011).
35. E. D. Palik, *Handbook of Optical Constants of Solids* (Academic, Cambridge, 1998).
36. M. A. Ordal, R. J. Bell, R. W. Alexander, L. A. Newquist, and M. R. Querry, "Optical properties of Al, Fe, Ti, Ta, W, and Mo at submillimeter wavelengths," Appl. Opt. **27**, 1203–1209 (1988).
37. E. H. Sondheimer, "The mean free path of electrons in metals," Adv. Phys. **1**, 1–42 (1952).
38. C. Z. Tan, "Determination of refractive index of silica glass for infrared wavelengths by IR spectroscopy," J. Non-Cryst. Solids **223**, 158–163 (1998).
39. T. J. Bright, J. I. Watjen, Z. M. Zhang, C. Muratore, A. A. Voevodin, D. I. Koukis, D. B. Tanner, and D. J. Arenas, "Infrared optical properties of amorphous and nanocrystalline Ta_2O_5 thin films," Appl. Phys. Lett. **114**, 083515 (2013).

1. Introduction

Research in electromagnetic absorbers has a long history, dating back to the Salisbury absorber in 1952 [1]. The development of negative refractive index metamaterials was a breakthrough in this technology. Negative index materials were first conceived by Vesalago in 1968 [2], but it was not until the year 2000 that an experimental demonstration was obtained [3]. Subwavelength structures to produce a desired electromagnetic response in materials and devices continues to be a subject of considerable interest. Along with many possible exotic electromagnetic effects, metamaterials can be optimized for perfect absorption. The first such metamaterial absorber was developed in 2008 [4], experimentally achieving 88% absorptance at microwave frequencies.

Optics EXPRESS

Similar absorbers in the terahertz (THz) [5], infrared (IR) [6] and visible [7] regions followed soon thereafter. The applications of these materials are widespread and include solar light harvesting [8], thermophotovoltaic cells [9], selective thermal emitters [10], optoelectronic devices [11], plasmonic sensors [12], and stealth applications [13]. The first generation of metamaterial absorbers was based on split ring resonance or electric ring resonance mechanisms, but this approach is difficult to implement in practice as the wavelength becomes shorter. More recently, based on a better understanding of photonic crystals and nano-scale fabrication, new and improved metamaterials to obtain specialized absorption spectra across a wider frequency range have been studied. Polarization-independent, ultra-broadband absorption, which is the focus of this study, has been achieved in the gigahertz (GHz) [14] and terahertz (THz) [15] regime using metamaterials. However, producing similar effects in the visible and near-IR regions using efficient and cost effective means is still a challenge. This paper describes a realistic approach to meet this challenge.

Recent studies into stratified metal-dielectric metamaterials have uncovered an efficient means of absorbing light at ultraviolet to near-infrared wavelengths [16,17]. Consider a periodic sequence of elementary cells comprised of a thin metal layer sandwiched between two identical dielectric layers. Such a stratified, symmetric elementary cell acts as an equivalent bulk material with a single effective characteristic impedance and Bloch wave-vector [18]. If the impedance of these metamaterials is matched to that of free space (incidence medium), all incident radiation will enter the material. The metal layers then absorb the radiation through ohmic loss [17]. Any number of the elementary cells may be stacked on top of each other depending on the thickness and performance requirements, as shown in Fig. 1(a). The fabrication of these metamaterials can be achieved using simple, low cost techniques like thermal evaporation or standard sputtering [19].

Impedance-matched metamaterials are inherently non-resonant absorbers, active over a broad bandwidth; however, the reflectivity of the metal layers dominates over the absorption as we venture deeper into the infrared region. In such a case, it seems reasonable to hypothesize that an effective anti-reflection coating would further improve the bandwidth and peak absorptance. The introduction of some amount of air to improve impedance-matching in flat surfaces has proven to be an effective strategy for designing extremely dark materials [20] and chemical sensors [21]. Another way to achieving impedance-matching is by imprinting “moth-eye” structures, shown in Fig. 1(b), through the top few elementary cells.

In the 1960s [22], it was discovered that corneal nipple patterns in the eyes of insects, and more specifically nocturnal moths, help them see clearly in the dark while also avoiding predation [23]. Later, with the advent of better fabrication technology, biomimetic structures based on this design were found to be effective in reducing Fresnel reflections at the interface [24]. Similar designs can be used to obtain layers of very high transmissivity [25] and for the suppression of thin-film interference [26]. These moth-eye surfaces have recently also been demonstrated to reduce coupling losses at the end faces of optical fibers [27] as well as the reflection glare for modern electronic displays [28]. They can be imprinted on an existing material using laser writing [29] or nanoimprint lithography [25,30] and directly imprinted on flat impedance-matched metamaterials.

In this study, we approximate these structures as truncated cones shown in Fig. 1(a), which are arranged as shown in Fig. 1(b). At wavelengths longer than the dimensions of the moth-eye structures, these surfaces can be simply modeled and reduce reflection by producing a gradual refractive index gradient at the interface. However, when the dimensions of these structures are on the order of the wavelength of the incident light, full-wave computational methods must be employed in order to model their reflection, transmission and absorption properties accurately. For the results that follow, we have used our own implementation of the rigorous coupled-wave algorithm (RCWA) [31–34], which is one of the fastest and most accurate methods for Fourier analysis of Maxwell’s equations when applied to moth-eye structures [27]. We consider incident

Optics EXPRESS

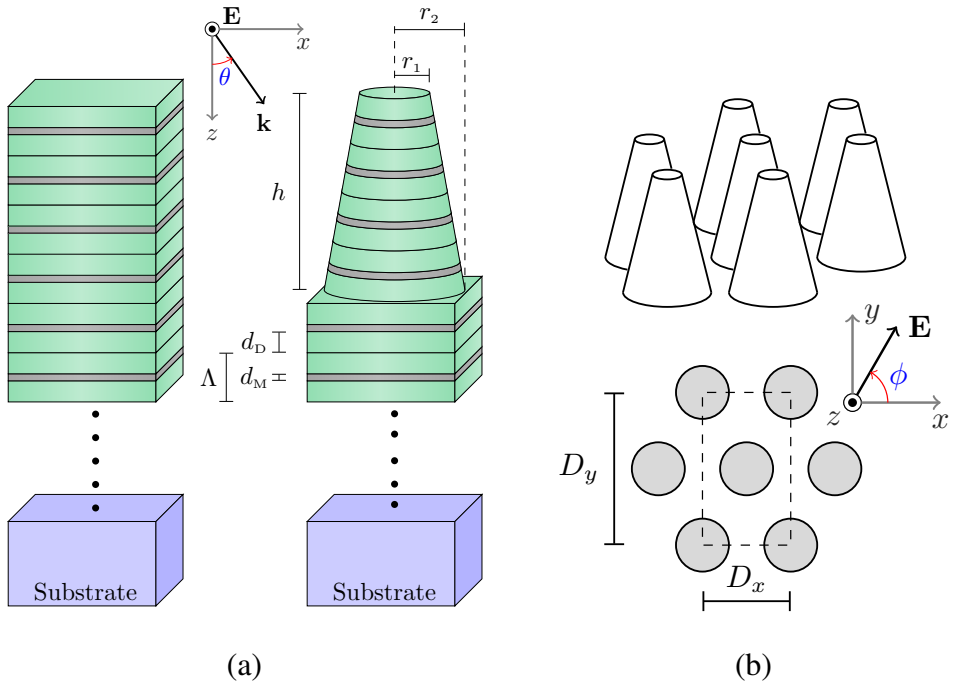

Fig. 1. Schematic illustrations of the metamaterial and incidence geometry. (a) Lateral view of impedance matched metal-dielectric metamaterials with a flat surface (left) and a moth-eye surface (right). The elementary cell has a period Λ and consists of a metal layer of thickness d_M sandwiched between dielectric layers of thickness d_D. For the truncated conical pillars that form the moth-eye surface (right), r_1 and r_2 are the radius at the top and bottom respectively and h is the height of the pillars. The incidence geometry for TE-polarized incidence is also shown. (b) Top and 3D views of the moth-eye structures that are obtained by arranging the truncated conical pillars in a triangular lattice with periods D_x and $D_y = \sqrt{3}D_x$ in the x- and y-directions respectively. The polarization angle ϕ is shown here for normal incidence.

light over a range of incident angles θ from 0° to 90° and polarization angles ϕ from 0° to 90°, as shown schematically in Fig. 1. The angle $\phi = 0°$ corresponds to TM waves; the angle $\phi = 90°$ corresponds to TE waves; intermediate angles of ϕ correspond to hybrid waves.

In the following section, we discuss the design of an improved metamaterial by combining the concept of impedance matched metallo-dielectric metamaterials [17] and anti-reflective moth-eye structures. We show the possibility of achieving broad-angle, polarization independent absorbers over an extremely broad frequency range from 400 nm to 6 μm.

2. Results and discussion

We now show that imprinting moth-eye structures on the first few layers of impedance matched metamaterials significantly broadens the material's absorptance spectrum. We model two impedance matched metal-dielectric metamaterials, one with the moth-eye surface and the other with a flat surface. We simulate the effects of monochromatic incidence from $\theta = 0°$ to $\theta \approx 90°$ on these metamaterials, and we plot the absorptance spectrum, shown in Fig. 2.

The metamaterial with a flat surface is the same as sample 2 from [17]. It consists of 10 repetitions of the elementary cell made up of a 10-nm layer of copper (Cu) between 30-nm

Optics EXPRESS

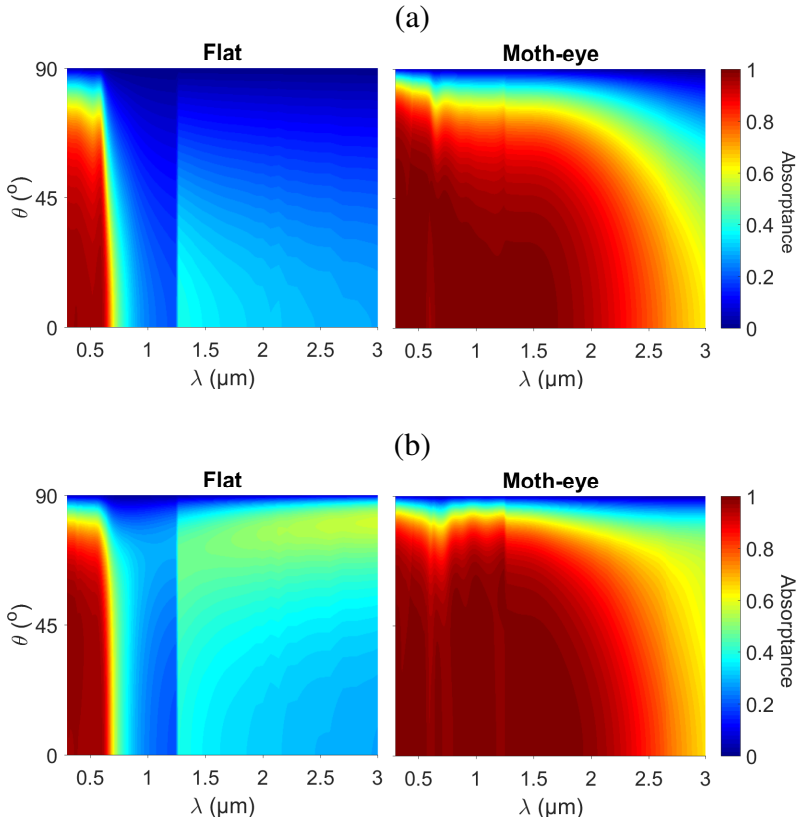

Fig. 2. The absorptance spectrum for the Cu-based metamaterial that we consider with (a) TE-polarized incidence ($\phi = 90°$) and (b) TM-polarized incidence ($\phi = 0°$). The elementary cell in this metamaterial has metal layers with thickness $d_M = 10$ nm and SiO_2 layers with thickness $d_D = 30$ nm. The moth-eye surface has a height $h = 280$ nm, periods $D_x = 300$ nm and $D_y = 520$ nm, and radii $r_1 = 50$ nm and $r_2 = 145$ nm.

layers of SiO_2 ($\Lambda = 70$ nm) on a quartz substrate with an index of refraction $n = 1.52$. The dispersion of quartz is negligible over the bandwidth of interest. The moth-eye metamaterial has its first 4 repetitions of the elementary cell imprinted into truncated pillars and arranged on a triangular lattice to form the moth-eye surface. The lattice periods are chosen as $D_x = 300$ nm and $D_y = 520$ nm, while the radii at the top and bottom are taken as 50 nm and 145 nm, respectively.

We chose our geometrical parameters using a standard design for moth-eye structures [27]. The base of the truncated cones is nearly touching their closest neighbors and the radii at the top is much smaller than the radii at the bottom which produces smoother impedance-matching than a flat surface. We found that the absorptance spectrum of impedance-matched metamaterials is not significantly altered by changing the design of the pillars as long as the thickness increases by more than a factor of 1.5 from top to bottom.

Along with Cu, we also consider metamaterials with tungsten (W) as the metal. The absorptance spectrum for these metamaterials is shown in Fig. 3. The elementary cell based on W is made of a 5 nm layer of the metal surrounded by 75 nm layers of Ta_2O_5. Since the flat metamaterial based on W is known to have a longer central wavelength and broader spectrum than the Cu-based metamaterial, the lattice periods are chosen to be $D_x = 834$ nm and $D_y = 1444$ nm. The radii are

Optics EXPRESS

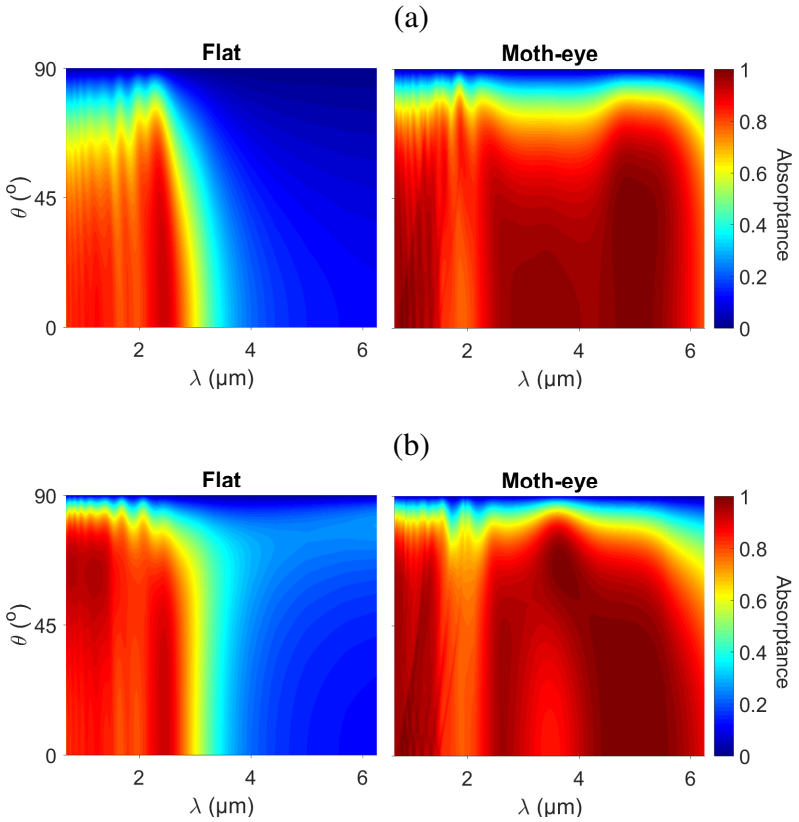

Fig. 3. The absorptance spectrum for the W-based metamaterial that we consider with (a) TE-polarized incidence ($\phi = 90°$) and (b) TM-polarized incidence ($\phi = 0°$). Structure parameters are: $d_M = 5$ nm, $d_D = 75$ nm, $h = 620$ nm, $D_x = 834$ nm, $D_y = 1444$ nm, $r_1 = 236$ nm, and $r_2 = 383$ nm.

similarly adjusted with $r_1 = 236$ nm and $r_2 = 383$ nm. No substrate is present, and the output medium is air with an index of refraction $n = 1$.

We use the data of Palik [35] and Ordal *et al.* [36] to obtain the dispersion of Cu and W respectively. Since the thickness of the metal layers is on the order of the electron mean free path, the Fuchs-Sondheimer theory [37] should be used for the Drude model calculations. Hence, the data for the bulk metals has been adjusted for thin metal films using the methodology elaborated in [17]. We also note that the sharp discontinuity in spectrum that we find at 1.25 μm in Fig. 2 arises from a discontinuity in Palik's data for the permittivity of Cu [35]. This discontinuity is due to Palik's use of two different sources for the data. The refractive index for SiO_2 comes from the Sellmeier equation [38] and for Ta_2O_5 from [39]. The plots for the metamaterials with a flat surface closely match the results shown in [17, Figs. 9–10], and the absorptance spectrum with the moth-eye surfaces is greatly broadened as anticipated. The TE and TM absorptance spectra are similar, although differences at high incidence angles are visible. From the similarity of these spectra, we conclude that the absorptance spectrum does not depend significantly on the polarization angle except at high incidence angles. In Fig. 4, to further support this conclusion, we show the absorptance spectra for several polarization angles.

To better understand the impact of impedance matching and anti-reflection, we also show the absorptance spectrum for all metal films, as well as metal moth-eye structures that are imprinted

Optics EXPRESS

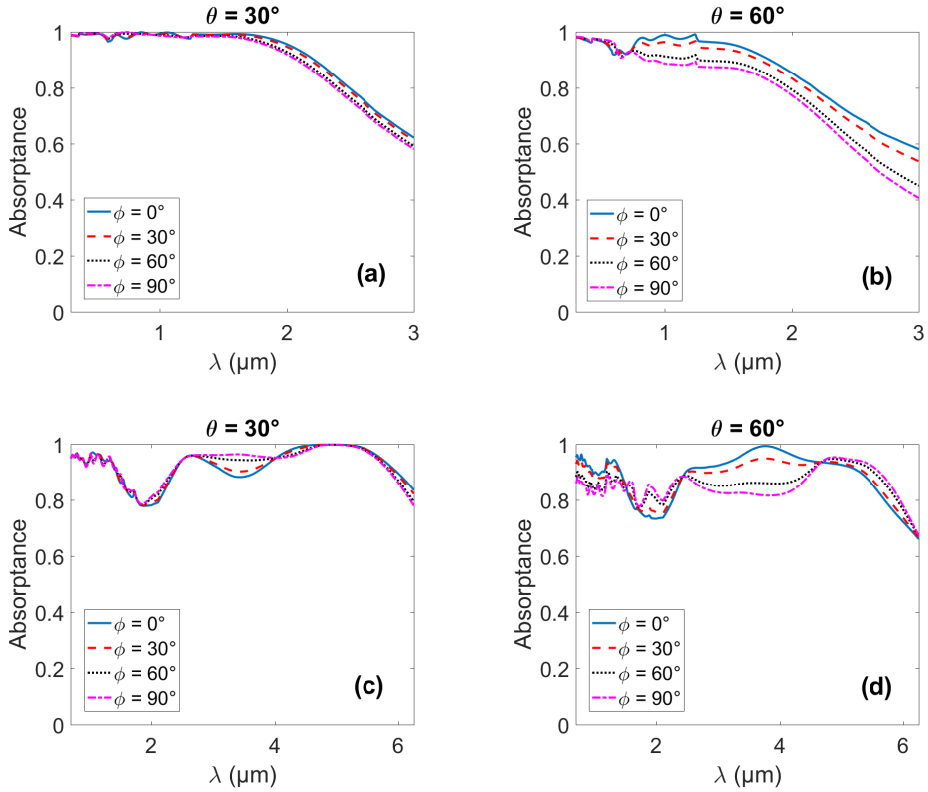

Fig. 4. Polarization dependence of the absorptance spectrum for the (a) and (b) Cu-based metamaterial, and for the (c) and (d) W-based metamaterial.

on a substrate of the same metal as the transmission medium in Fig. 5. The dimensions of these materials, like the thickness of the film, radii and periods of the moth-eyes are equivalent to their corresponding metal-dielectric structures. We find a much weaker absorptance profile for the metal films and no significant broadening with the metal moth-eye surfaces. We conclude that the ultra-broadband absorption that is shown in Figs. 2 and 3 is not just due to the metal or moth-eye surface, but due to a combination of impedance-matched metal-dielectric metamaterials and the moth-eye surface. A clearer picture on how that happens can be obtained by examining the field distribution inside the metamaterials.

In Figs. 6 and 7, we show the intensity of the electric field and the ohmic loss [$\mathrm{Im}(\epsilon)\,|\mathrm{E}|^2$] distribution within the metamaterials. We focus on two incident wavelengths each for the Cu-based and W-based metamaterials. These wavelengths are chosen such that the shorter wavelength lies within the absorptance spectrum of the flat as well as moth-eye metamaterial. The other wavelength is absorbed only by the moth-eye metamaterial. We chose wavelengths of 0.5 μm, and 1.2 μm for the Cu-based metamaterials, and we choose 2.5 μm, and 5 μm for the W-based metamaterial.

We find that the field intensity drops to zero before the metamaterial region ends. This means that no transmission of light occurs and all unabsorbed radiation is reflected. In the flat metamaterial, the maximum attenuation always occurs in the first metal layer and successively decreases with each layer. Moreover, the peak absorptance in the first metal layer is not significantly reduced even at the longer wavelength. However, the penetration is hampered because the first layer has

Optics EXPRESS

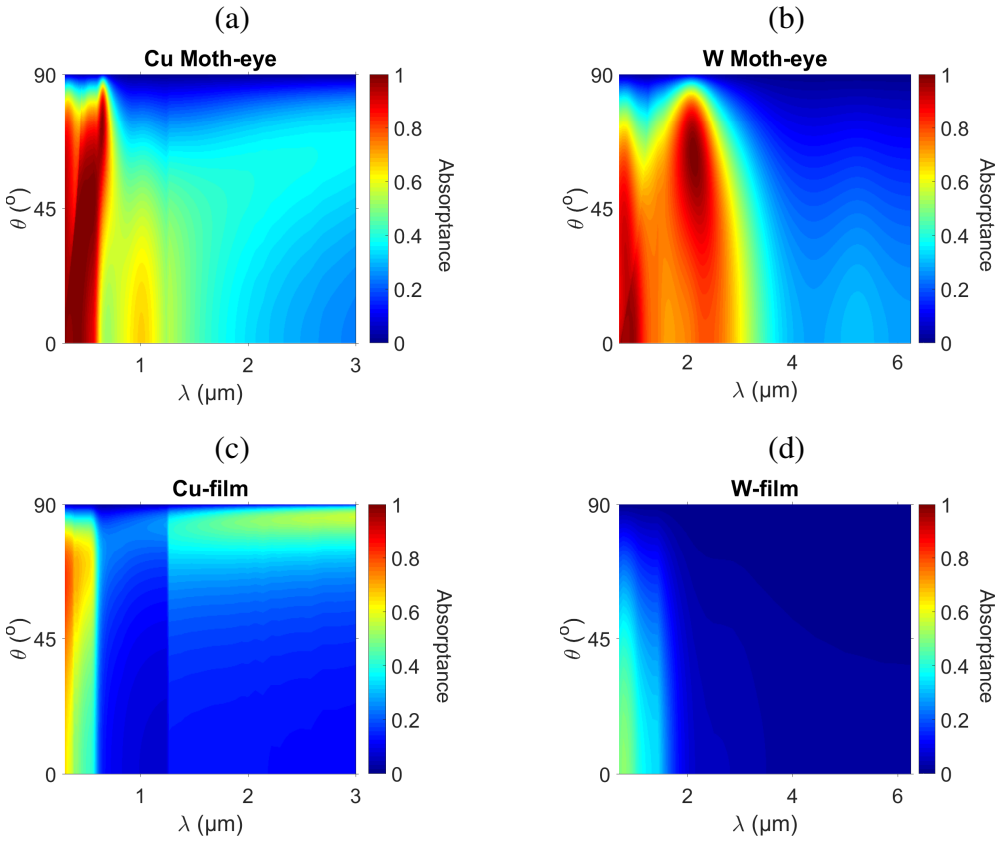

Fig. 5. The absorptance spectrum for the non-impedance-matched all-metal films and moth-eye structures. (a) Moth-eye surfaces made entirely of Cu with TM-polarized incidence. (b) Moth-eye surfaces made entirely from W with TE-polarized incidence. (c) 700-nm thick Cu-film with TM polarized incidence. (d) 1550-nm thick W-film with TE-polarized incidence. The dimensions for the moth-eye surfaces are outlined in Fig. 2(a) for (a) and Fig. 3(a) for (b) with a transmission region that consists of the same metal. Transmission region for (c) and (d) is air.

Optics EXPRESS

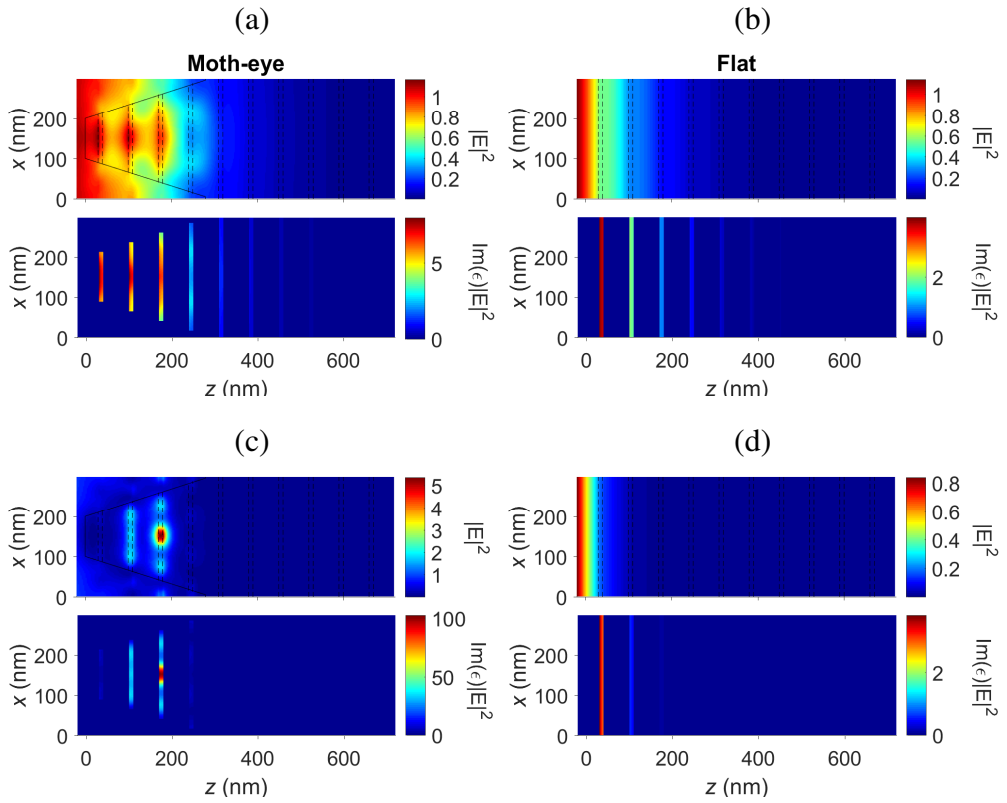

Fig. 6. Electric field intensity and ohmic loss distribution for Cu-based metamaterials. (a) $\lambda = 0.5$ µm. Absorptance > 99%. (b) $\lambda = 0.5$ µm. Absorptance ≈ 95%. (c) $\lambda = 1.2$ µm. Absorptance ≈ 99%. (d) $\lambda = 1.2$ µm. Absorptance ≈ 20%.

now reflected much of the light, and the energy carried by it never reaches the other metal layers, which are shown by the broken lines in Figs. 6 and 7. Hence, the total absorption is reduced.

For the moth-eye surface we look at the fields in a plane dividing the pillars in two vertical halves. The solid line traces the projection of the truncated pillars on this plane. In this case, the moth-eye surface act like a lens, focusing the incident energy at just a few spots inside the structure. Hence, a greater amount of energy passes through the metal, which produces higher loss that is also heavily concentrated in a few layers.

3. Conclusion

We have proposed and computationally analyzed a novel approach to achieve absorption over a wide spectrum by combining two independent mechanisms: (a) metal-dielectric impedance-matched metamaterials and (b) anti-reflective moth-eye structures. The analysis was done using the RCWA method, which was developed in-house and validated by comparison with experimental results. Our implementation was then applied to the proposed designs.

By testing the hypothesis on structures that were designed using the metals Cu and W, we found that moth-eye surfaces imprinted on impedance-matched metal-dielectric metamaterials can greatly broaden the absorption bandwidth of the corresponding flat metamaterial. By simulating the absorptance spectrum of metal films and moth-eye structures, we also confirmed that neither the metal nor the moth-eye structures alone are the cause of the broadening. Finally, by generating

Optics EXPRESS

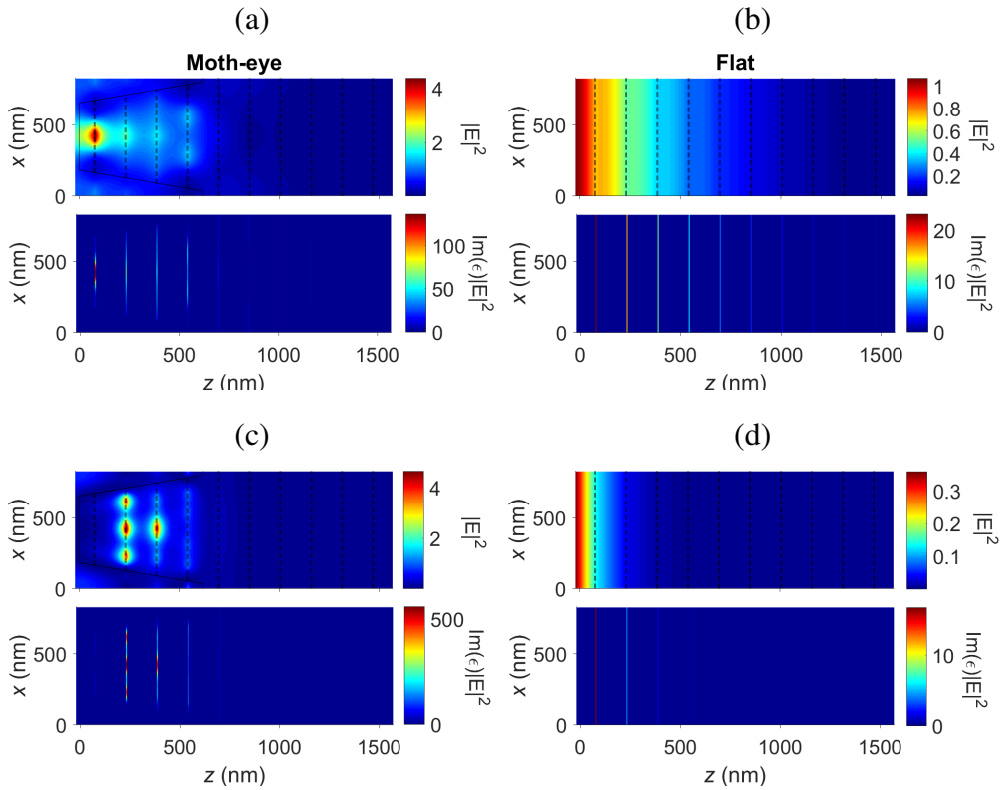

Fig. 7. Electric field intensity and ohmic loss distribution for W-based metamaterials. (a) $\lambda = 2.5$ μm. Absorptance ≈ 90%. (b) $\lambda = 2.5$ μm. Absorptance ≈ 90%. (c) $\lambda = 5$ μm. Absorptance > 99%. (d) $\lambda = 5$ μm. Absorptance ≈ 15%.

a visual representation of the electric field distribution inside the metamaterials, we provided an understanding of the loss mechanism behind this phenomenon.

We have computationally demonstrated a practical and cost efficient approach to obtain polarization-independent, non-resonant, broadband absorption. Similar to flat impedance-matched metamaterials, the absorption of the moth-eye metamaterial is also independent of the substrate and can be used as a thin film to cover other materials. The fabrication of planar multilayer materials can be achieved through standard sputtering or thermal evaporation techniques [19], and fabrication of moth-eye structures based on nanopillars with dimensions on the order of a few hundreds of nm is well within the reach of current nanolithography techniques. Moreover, while here we have used metals, the same concepts and designs can be exploited using semiconductor materials in their absorption band. In this case, instead of being dissipated through ohmic losses in the metal, the light can be harvested to create electron-hole pairs in the semiconductor material for efficient infrared detectors, night vision cameras, or solar cell applications.

Appendix

The rigorous coupled-wave algorithm (RCWA) is a semi-analytical Fourier space method that can be used to find exact solutions for electromagnetic waves diffracted through a dielectric grating. In this appendix we aim to summarize the key aspects of this approach [31–34].

We first consider the propagation of light through a thin layer whose permittivity $\epsilon = \epsilon(x, y)$ is independent of z. We will later show how to combine multiple such layers to determine the

Optics EXPRESS

entire propagation. The single permittivity layer divides the space into 3 parts. The incident light is assumed to be a unit amplitude, monochromatic electromagnetic plane wave with free space wavelength λ_0. This wave, travelling from the half space $z < 0$ (region 1) at an arbitrary angle with respect to the z-direction is incident on this thin permittivity distribution of finite thickness h along the (x, y) plane. The incident electric field from such a plane wave at any point with $z < 0$ can be written as,

$$\boldsymbol{E}_{\text{inc}}(\boldsymbol{r}) = \exp(-j\boldsymbol{k}_{\text{inc}} \cdot \boldsymbol{r})\, \hat{\mathbf{u}} \qquad \forall\, \boldsymbol{r} \;\mid\; z < 0, \tag{1}$$

where $\hat{\mathbf{u}}$ is the polarization vector and $\boldsymbol{k}_{\text{inc}}$ is the incident wave vector, $\boldsymbol{k}_{\text{inc}} = k_{x0}\,\hat{\mathbf{x}} + k_{y0}\,\hat{\mathbf{y}} + k_{1,z00}\,\hat{\mathbf{z}}$. The reflected and transmitted fields are expressed in term of amplitude coefficients $\boldsymbol{R}_{mn}$, and $\boldsymbol{T}_{mn}$ of the mnth Fourier series component.

$$\boldsymbol{E}_{\text{R}}(\boldsymbol{r}) = \sum_{m,n} \boldsymbol{R}_{mn}\ \exp(j\boldsymbol{k}_{1,mn} \cdot \boldsymbol{r}), \tag{2a}$$

$$\boldsymbol{E}_{\text{T}}(\boldsymbol{r}) = \sum_{m,n} \boldsymbol{T}_{mn}\ \exp(j\boldsymbol{k}_{3,mn} \cdot \boldsymbol{r}), \tag{2b}$$

Here m and n are integers from $-N_x$ to N_x, and $-N_y$ to N_y respectively, and the number of diffracted modes to be included in the computations are N_x and N_y in the x- and y-directions respectively. The wavevector corresponding to the mnth component for the homogeneous regions $\rho = 1, 3$ is $\boldsymbol{k}_{\rho,mn} = k_{xmn}\,\hat{\mathbf{x}} + k_{ymn}\,\hat{\mathbf{y}} - k_{\rho,zmn}\,\hat{\mathbf{z}}$ where the x- and y-components are expanded as

$$k_{xmn} = k_{x0} + 2\pi m/D_x, \tag{3a}$$

$$k_{ymn} = k_{y0} + 2\pi n/D_y, \tag{3b}$$

The z-component follows from orthonormality, while D_x and D_y is the periodicity of the permittivity distribution in the x- and y-direction respectively. The magnetic field can be expressed using a normalized form of Maxwell's curl equation $k_0\boldsymbol{H} = \boldsymbol{\nabla} \times \boldsymbol{E}$. The matrices $\mathbf{R} = [\boldsymbol{R}_{mn}]$ and $\mathbf{T} = [\boldsymbol{T}_{mn}]$ of size $(2N_x+1)\times(2N_y+1)$ can be reshaped to a $(2N_x+1)(2N_y+1)\times 1$ column vector so that the x- and y-components of the field magnitudes can be arranged as a column vector $\mathbf{E} = \begin{bmatrix}\mathbf{E}_x & \mathbf{E}_y\end{bmatrix}^{\text{T}}$. The relationship between the electric and magnetic field can now be expressed concisely as

$$\mathbf{H} = \mathbf{V}_\rho \mathbf{E}, \tag{4}$$

where $\mathbf{V}_\rho$ is the matrix form of the curl operator and is dependent on the permittivity of the region ρ.

Inside the permittivity distribution, Maxwell's equations are coupled. Expanding the equations in terms of the spatial components and eliminating the z-component, we obtain

$$\begin{aligned}
\partial_z E_x &= k_0 H_y + \partial_x[(k_0\epsilon)^{-1}(\partial_x H_y - \partial_y H_x)],\\
\partial_z E_y &= -k_0 H_x + \partial_y[(k_0\epsilon)^{-1}(\partial_x H_y - \partial_y H_x)],\\
\partial_z H_x &= k_0\epsilon E_y + \partial_x[(k_0)^{-1}(\partial_x E_y - \partial_y E_x)],\\
\partial_z H_y &= -k_0\epsilon E_x + \partial_y[(k_0)^{-1}(\partial_x E_y - \partial_y E_x)],
\end{aligned} \tag{5}$$

where ∂_l denotes the partial derivative with respect to l.

Once the permittivity distribution is expanded as a two-dimensional Fourier series using the rules outlined by Li [33], the set of partial differential equations, Eq. (5), can be rewritten in matrix form using $\mathbf{F}$ and $\mathbf{G}$ as

$$\partial_z \mathbf{E} = k_0 \mathbf{F}\mathbf{H}, \tag{6a}$$

Optics EXPRESS

$$\partial_z \mathbf{H} = k_0 \mathbf{G}\mathbf{E}\,. \tag{6b}$$

The mathematical form for $\mathbf{F}$ and $\mathbf{G}$ can be found in [33]. Eliminating $\mathbf{H}$, we arrive at an eigenvalue equation

$$\partial_z^2 \mathbf{E} = k_0^2 \mathbf{F}\mathbf{G}\mathbf{E}, \tag{7}$$

which is solved by diagonalizing the matrix $\mathbf{FG} = \mathbf{W}\boldsymbol{\Gamma}^2\mathbf{W}^{-1}$, where $\boldsymbol{\Gamma}$ is a diagonal matrix with the square roots of the eigenvalues of $\mathbf{FG}$ in its diagonal elements. The corresponding eigenvectors are the columns of $\mathbf{W}$. As a result, Eq. (7) is simplified to

$$\partial_z^2(\mathbf{W}^{-1}\mathbf{E}) = (k_0\boldsymbol{\Gamma})^2(\mathbf{W}^{-1}\mathbf{E}), \tag{8}$$

and has the solution

$$\mathbf{E}(z) = \mathbf{W}\begin{bmatrix} \boldsymbol{\Phi}(z)\,\mathbf{c}^+ \\ \mathbf{X}\boldsymbol{\Phi}(-z)\,\mathbf{c}^- \end{bmatrix}, \tag{9}$$

where $\boldsymbol{\Phi}(z) = \exp(-k_0\boldsymbol{\Gamma}z)$ and $\mathbf{X} = \boldsymbol{\Phi}(h)$.

The eigenvectors in $\mathbf{W}$ are the fundamental modes of the permittivity distribution $\epsilon(x, y)$ and do not change shape as they travel through it. The corresponding eigenvalues in $\boldsymbol{\Gamma}$ give the propagation constant and $\boldsymbol{\Phi}(z)$ propagates these modes by a distance z. The column matrices $\mathbf{c}^+$ and $\mathbf{c}^-$ comprise of the unknown amplitudes of these eigenmodes in the forward and backward travelling waves respectively. A similar solution for the magnetic field is obtained from (6b) by defining $\mathbf{V} = -\mathbf{G}\mathbf{W}\boldsymbol{\Gamma}^{-1}$. Combining the fields in a single equation yields

$$\begin{bmatrix} \mathbf{E}(z) \\ \mathbf{H}(z) \end{bmatrix} = \begin{bmatrix} \mathbf{W} & \mathbf{W} \\ \mathbf{V} & -\mathbf{V} \end{bmatrix} \begin{bmatrix} \boldsymbol{\Phi}(z) & \mathbf{0} \\ \mathbf{0} & \mathbf{X}\boldsymbol{\Phi}(-z) \end{bmatrix} \begin{bmatrix} \mathbf{c}^+ \\ \mathbf{c}^- \end{bmatrix}. \tag{10}$$

The fields in the homogeneous regions can also be expressed as a similar expression where $\mathbf{W}_\rho$ becomes the identity matrix and $\mathbf{V} = \mathbf{V}_\rho$ for region ρ. By applying the boundary conditions at $z = 0$ and $z = h$, we can solve for $\mathbf{c}^+$ and $\mathbf{c}^-$ within the permittivity distribution, and, $\mathbf{R}$ and $\mathbf{T}$ for the reflected and transmitted waves. Thus enabling us to reconstruct the field distribution and compute the reflection, transmission and absorption efficiency.

For multi-layered gratings such as those investigated here, the individual layers are combined to form a scattering (S) matrix $\mathbf{S}$, which defines the response of the entire structure. If the amplitude coefficients of the eigenmodes in the incident wave are given by $\boldsymbol{\delta}$, the reflected and transmitted coefficients, $\mathbf{R}$ and $\mathbf{T}$ can then be computed by

$$\begin{bmatrix} \mathbf{T} \\ \mathbf{R} \end{bmatrix} = \mathbf{S}\begin{bmatrix} \delta \\ \mathbf{0} \end{bmatrix}. \tag{11}$$

For a permittivity distribution made up of N_z different regions (including the incidence and transmission region), the boundary condition at the ℓth interface ($0 < \ell < N_z$) can be expressed as

$$\begin{bmatrix} \mathbf{W}_\ell\mathbf{X}_\ell & \mathbf{W}_\ell \\ \mathbf{V}_\ell\mathbf{X}_\ell & -\mathbf{V}_\ell \end{bmatrix} \begin{bmatrix} \mathbf{c}_\ell^+ \\ \mathbf{c}_\ell^- \end{bmatrix} = \begin{bmatrix} \mathbf{W}_{\ell+1} & \mathbf{W}_{\ell+1}\mathbf{X}_{\ell+1} \\ \mathbf{V}_{\ell+1} & -\mathbf{V}_{\ell+1}\mathbf{X}_{\ell+1} \end{bmatrix} \begin{bmatrix} \mathbf{c}_{\ell+1}^+ \\ \mathbf{c}_{\ell+1}^- \end{bmatrix}. \tag{12}$$

This can be rearranged in the form an S-matrix equation $\begin{bmatrix} \mathbf{c}_{\ell+1}^+ & \mathbf{c}_\ell^- \end{bmatrix}^{\mathrm{T}} = \mathbf{s}_\ell \begin{bmatrix} \mathbf{c}_\ell^+ & \mathbf{c}_{\ell+1}^- \end{bmatrix}^{\mathrm{T}}$, and we obtain a single-interface S-matrix,

$$\mathbf{s}_\ell = \begin{bmatrix} \mathbf{W}_{\ell+1} & -\mathbf{W}_\ell \\ \mathbf{V}_{\ell+1} & \mathbf{V}_\ell \end{bmatrix}^{-1} \begin{bmatrix} \mathbf{W}_\ell\mathbf{X}_\ell & -\mathbf{W}_{\ell+1}\mathbf{X}_{\ell+1} \\ \mathbf{V}_\ell\mathbf{X}_\ell & \mathbf{V}_{\ell+1}\mathbf{X}_{\ell+1} \end{bmatrix}. \tag{13}$$

Optics EXPRESS

The advantage of this formulation is that the behavior of two stacked interfaces can be consolidated by applying the Redheffer star product [34], usually denoted by the $\star$ operator, between the S-matrices of the interfaces. The complete S-matrix for a system with $N_z - 1$ interfaces is thus given by

$$\mathbf{S} = \mathbf{s}_1 \star \mathbf{s}_2 \star \cdots \star \mathbf{s}_{N_z-1} . \tag{14}$$

Funding

Army Research Laboratory (W911NF-13-2-0010); Naval Research Laboratory (N00173-15-1-G905).